AIAA 96-2540

An Experimental and Computational Investigation of a Translating Throat Single Expansion-Ramp Nozzle

K. A. Deere and S. C. Asbury
NASA Langley Research Center
Hampton, VA

32nd AIAA/ASME/SAE/ASEE
Joint Propulsion Conference & Exhibit
July 1-3, 1996 / Lake Buena Vista, FL

An Experimental and Computational Investigation of a Translating Throat Single Expansion-Ramp Nozzle

Karen A. Deere† and Scott C. Asbury†
NASA Langley Research Center
Hampton, Virginia

ABSTRACT

A translating throat single expansion-ramp nozzle (SERN) concept was designed to improve the off-design performance of a SERN with a large, fixed expansion ratio. The concept of translating the nozzle throat provides the SERN with a variable expansion ratio. An experimental and computational study was conducted to predict and verify the internal performance of this concept. Three nozzles with expansion ratios designed for low, intermediate, and high Mach number operating conditions were tested in the Jet-Exit Test Facility at the NASA Langley Research Center. Each nozzle was tested with a concave and a convex geometric expansion ramp surface design. Internal nozzle performance, paint-oil flow and focusing Schlieren flow visualization were obtained for nozzle pressure ratios (NPRs) up to 13. The Navier-Stokes code, PAB3D, with a k-ε turbulence model was utilized to verify experimental results at selected NPRs and to predict the performance at conditions unattainable in the test facility. Two-dimensional simulations were computed with near static free-stream conditions and at nozzle pressure ratios of 5, 9, and 13 for the concave ramp, low Mach number configuration and at the design NPR of 102 for the concave ramp, high Mach number configuration. Remarkable similarities between predicted and experimental flow characteristics, as well as performance quantities, were obtained.

INTRODUCTION

The importance of the propulsion system for future high-speed (Mach 4 to 6) cruise aircraft and single-stage-to-orbit aerospace vehicles has provided the impetus for studies focused on performance comparisons of axisymmetric nozzles, single expansion-ramp nozzles (SERN), and two-dimensional convergent-divergent (2DCD) nozzles. As a result of the extended operating range of these vehicles, pressure ratios up to 600 (refs. 1-2), nozzle expansion ratios (A_e/A_t) of up to 27 are required to assure maximum internal performance. Current variable geometry, axisymmetric and 2DCD nozzle designs are undesirable due to the mechanical limitations of the flap and seal arrangement that limit their maximum expansion ratio to approximately 3.6 (refs. 1-2). Single expansion-ramp nozzles have a unique installation advantage because the underside of the vehicle's afterbody can be used as an external expansion ramp to achieve very high nozzle expansion ratios (fig. 1). Since SERN nozzles have a much shorter lower flap compared to equivalent performing 2DCD nozzles, their integration also offers significant reduction in propulsion system weight penalties.

Past studies of single expansion-ramp nozzles with one fixed design point for high-speed flight conditions indicate that SERN nozzles suffer significant performance penalties at off-design conditions (ref. 3). Maximum propulsive efficiency of SERN nozzles is highly dependent on nozzle pressure ratio and nozzle expansion ratio (refs. 4-6). High-speed SERN applications are designed with large expansion ratios which are necessary for maximum performance at high speeds and altitudes. However, at subsonic and transonic flight conditions the expansion ratio is too large to maintain attached, fully expanded flow along the entire length of the expansion ramp. Consequently, the exhaust flow overexpands and separates from the upper expansion ramp resulting in substantial penalties due to afterbody pressure drag, decreased nozzle thrust and decreased propulsive efficiency.

†Aerospace Engineer, Component Integration Branch

The translating throat SERN concept, conceived to improve the off-design performance of a high speed SERN application with a large expansion ratio, was the focus of the present study. The goal of translating the axial throat location was to maintain maximum performance by providing a variable expansion ratio and allowing a more optimum exhaust expansion at various flight conditions. An illustration of the translating throat concept integrated into the afterbody of a high-speed vehicle is shown in figure 2. This concept may be adapted to different engine configurations and may include more than three doors (i.e. design points). A ramjet or scramjet engine is used for propulsion at high-speed flight conditions and the three doors in the underside of the afterbody are closed to form a long expansion ramp. During low-speed flight conditions, a gas turbine engine with a drop down inlet is used for propulsion; exhaust flow is discharged out an open door in the expansion ramp of the vehicle. To improve the performance at off-design conditions, three actuated doors are integrated into the expansion ramp to allow for changes in the expansion ratio.

A sketch of the experimental model tested during this study is shown in figure 3. The three geometric configurations illustrate three typical expansion ratios required for low, intermediate and high Mach number operating conditions. For take-off and low speed operation at subsonic and transonic flight conditions, door 1 is opened to divert the flow internally to a throat location near the end of the expansion ramp. This provides a small expansion ratio necessary for optimum expansion at low operating pressure ratios. As the vehicle gains speed and altitude, door 1 is closed and door 2 is opened at the intermediate throat location. This provides a larger expansion ratio for higher nozzle pressure ratios encountered in the low supersonic flight regime. At high supersonic flight conditions, door 2 is closed and door 3 is opened to form a larger expansion ratio necessary for optimum performance.

An experimental and computational study was conducted to determine the performance of this new SERN concept. A static (wind-off) experimental study was conducted in the NASA Langley Jet-Exit Test Facility to determine internal nozzle performance at nozzle pressure ratios up to 13. Six configurations were tested, including three expansion ratios and two geometric expansion ramp surface designs (one concave and one convex) for each expansion ratio. A Navier-Stokes code, PAB3D, with a two-equation, k-ε turbulence model was utilized to predict the performance of the concept at several experimental test conditions as well as one condition unattainable in the test facility. Nozzle performance characteristics were predicted at nozzle pressure ratios of 5, 9, and 13 for the concave ramp, low Mach number configuration, and at the design NPR (NPR_D = 102) of the concave ramp, high Mach number nozzle.

NOMENCLATURE

A_t	nozzle throat area, 2.0 in^2 nominal
A_e	nozzle exit area, in^2
F_A	measured axial thrust, lbf
F_N	measured normal force, lbf
F_i	ideal isentropic gross thrust, lbf
F_r	resultant gross thrust, $\sqrt{F_A^2+F_N^2}$, lbf
k	turbulent kinetic energy, Pa
L_{ref}	reference length of nozzle assembly, 16.9 in
M	free stream Mach number
MS	model station, in
N	unit normal vector, (n_1, n_2, n_3)
NPR	nozzle pressure ratio, $p_{t,j}/p_a$
NPR_D	design NPR based on external expansion ratio
p	local static pressure, psi
p_a	ambient pressure, psi
$p_{t,j}$	average jet total pressure, psi
p_∞	free stream static pressure, psi
U	velocity vector
w_i	ideal weight flow rate, lbf/sec
w_p	measured weight flow rate, lbf/sec
δ_p	resultant pitch thrust vector angle, $\tan^{-1}(F_N/F_A)$
ε	turbulent energy dissipation
ϕ_r	initial expansion ramp angle at the throat, deg
ρ	density, $slug/ft^3$

EXPERIMENTAL STUDY

Model

The translating throat nozzle model was tested at three expansion ratios (design points) to simulate configurations for low, intermediate, and high Mach number operating conditions as shown in figure 3. In addition, two geometric expansion ramp surface designs (one concave and one convex) were tested at each design point to provide a total of six nozzle configurations. Geometric parameters (including expansion ratios and design nozzle pressure ratios) are presented in Table 1 with sketches and a photograph of the model shown in figures 4 to 7.

Each nozzle configuration tested included a lower flap, a nozzle ramp assembly, a ramp insert, and two sidewalls to contain exhaust flow in the

lateral direction (see fig. 7). The 16.9 inch long nozzle ramp assembly was common to all configurations. Three lower flaps of lengths 12.7, 9, and 5.3 inches were used for the low, intermediate, and high Mach number configurations, respectively. Each nozzle was tested with two 10.88 inch long ramp inserts to compare nozzle performance with a concave and a convex expansion ramp geometry. A sketch of the concave and convex ramp surfaces near the throat of the low Mach number configuration is shown in figure 4. Each nozzle had a nominal throat area of 2 in^2 and a constant flow-path width of 5 inches.

Table 1. Geometric parameters of the translating throat nozzle model.

Design Point	Ramp Design	ϕ_r	A_e/A_t	NPR_D
Low Mach #	concave	-5.4	1.83	9.0
Intermediate Mach #	concave	-10	4.63	42.2
High Mach #	concave	-14.3	8.25	102.4
Low Mach #	convex	5.6	1.9	9.9
Intermediate Mach #	convex	-4.8	4.63	42.2
High Mach #	convex	1.8	8.59	109.1

Jet-Exit Test Facility

The experimental investigation was conducted in the Jet-Exit Test Facility at NASA Langley Research Center (LaRC). This facility is utilized to determine the internal performance of exhaust nozzles at jet-on, static (wind-off) conditions. Testing is conducted in a large room where the jet from a dual-flow single-engine propulsion simulation system vents to the atmosphere through an acoustically treated exhaust passage. A control room is remotely located from the test room, and a closed-circuit television is used to observe the model when the jet is operating. This static test facility has an air control system that is similar to that of the 16-Foot Transonic Tunnel at NASA LaRC and includes valving, filters, and a heat exchanger to maintain the jet flow at a constant stagnation temperature. The air system utilizes the same clean, dry air supply as that used by the 16-Foot Transonic Tunnel (ref. 7).

Propulsion Simulation System

The translating throat SERN model was tested on a dual-flow single-engine propulsion simulation system, which consists of an axisymmetric air-powered model mounted on a six-component strain-gauge balance attached to an A-frame structural support cart (fig. 5). A photograph of the high Mach number configuration installed on the dual-flow propulsion simulation system is shown in figure 6. An external high-pressure air system supplies the simulator with a continuous flow of clean, dry air at a constant stagnation temperature of approximately 540° R at the nozzle. Jet total pressure was varied from atmospheric pressure to 190 psi during jet simulation.

Independently controlled primary and secondary flow systems provide pressurized air to isolated plenum chambers in the dual-flow system through two pairs of semi-rigid, thin-walled (0.021 inches wall thickness), 1-inch diameter, S-shaped, stainless steel tubes (S-tubes). These tubes provide flexible connections which transfer air from the non-metric to the metric (supported by the force balance) part of the system. The geometric design of the airflow system acts to minimize any balance force and moment tares which can be generated by flexure of the S-tubes as air pressure is increased or by transfer of axial momentum as pressurized air passes into the plenums. The primary and secondary air systems can be used separately or combined for single- or dual-flow operation. For the current investigation, only the primary air system was used.

High-pressure air supplied to the primary plenum is delivered by a 30 lbf/sec air system that contains dual in-line venturis for weight-flow measurements. From the primary plenum, air is discharged radially into an annular low-pressure duct (positioned on the model centerline) through eight equally spaced sonic nozzles (fig. 7). The primary airflow then passes over an aerodynamic balance fairing, through a choke plate (primarily used as a flow straightener), a primary instrumentation section (used for balance calibrations), and through a transition section (used to transition the flow from an axisymmetric geometry to the rectangular geometry of the SERN nozzles). A choke plate is used at MS 30.25 to provide a uniform flow field into the instrumentation section of the SERN nozzle. Flow enters the SERN nozzle at model station 36.25 and exhausts to sea level static conditions at the trailing edge of the lower flap.

Instrumentation

All forces and moments were measured by a six-component strain-gauge balance located on the centerline of the dual-flow propulsion simulation system (fig. 7). The weight-flow rate of high-

pressure air supplied to the model was calculated from static-pressures and temperatures measured near or in the dual in-line venturis. Nozzle flow conditions were determined in the SERN instrumentation section with two five-probe total-pressure rakes offset 1.25 inches from the model centerline and one thermocouple located along the centerline. Jet total pressure ($p_{t,j}$) was determined by an average of the ten total pressure measurements. Each nozzle had twenty-nine static pressure orifices located along the upper expansion ramp (seventeen orifices along the centerline and twelve orifices offset 1.91 inches from the centerline).

Flow Visualization

Paint-Oil Flow

Nozzle internal flow visualization was obtained by using a mixture of linseed oil, tempera paint, and kerosene. The paint mixture was brushed onto the model surface across the flow direction so as not to leave a predetermined paint pattern inside the nozzle that could be misinterpreted as flow streamlines. Then, the propulsion simulation system was turned on and the jet-flow evaporated the kerosene, leaving a residue representing the surface flow patterns along the expansion ramp of the nozzle. Although analysis based on this type of flow visualization is fairly subjective, it can provide insight into the flow behavior on and near the painted surfaces (ref. 8).

Focusing Schlieren System

The requirements established by Weinstein (ref. 9) were used to determine optical specifications for the focusing Schlieren system located in the Jet-Exit Test Facility. The field of view dimensions were 330.2 mm x 431.8 mm with a 5.41 mm depth of sharp focus. Flow features larger than 0.2 mm were resolved along the focal plane, while features outside of a 53.16 mm unsharp focus depth were effectively blurred. The system has a sensitivity of 9.7 arcsec. A xenon strobe flash tube was used for a light source and a driving circuit detected the synchronized pulses from a recording video camera. The flash pulsed at a rate of 30 Hz with a power of 0.3 W·sec and had a flash duration of 1.2 μsec at one third peak power. Flow characteristics were recorded with a 70 mm Hasselblad still camera.

This system provided information about the density gradients of a "slice" of flow (defined above) located along the centerline of the expansion ramp which could be compared with computational fluid dynamic results.

Data Acquisition and Reduction

Each data point is the average steady-state value computed from 50 frames of data taken at a rate of 10 frames per second. All data were taken in ascending order of jet total pressure, $p_{t,j}$. Balance measurements were initially corrected for model weight tares and isolated-balance component interactions. Additional calibrations of the balance installed in the dual-flow system were performed to determine jet-off installation tares and to measure the effects of model pressurization and exhaust flow momentum. Although the S-tube geometry in the air system was designed to minimize balance effects due to pressurization and flow transfer, small tares resulted as the S-tubes deformed slightly under pressure. These tares were determined by testing single-engine calibration nozzles with known performance over ranges of expected internal pressure and external forces and moments. The jet-off and momentum/pressurization corrections were then applied to fully correct the balance data. A detailed description of the procedures used for data reduction and analysis in this investigation can be found in reference 10.

Four basic nozzle internal performance parameters were used in the presentation of results: internal axial thrust ratio F_A/F_i, resultant thrust ratio F_r/F_i, resultant pitch thrust vector angle δ_p and discharge coefficient w_p/w_i.

The internal axial thrust ratio is the ratio of measured axial force to ideal isentropic thrust. Ideal thrust F_i is based on measured weight flow w_p, jet total pressure $p_{t,j}$, and jet total temperature $T_{t,j}$. The resultant thrust ratio F_r/F_i is the ratio of resultant thrust to ideal isentropic thrust. Resultant thrust F_r is obtained from the measured axial, normal, and side force components of the jet resultant force. The internal axial thrust ratio includes a reduction in thrust that results from flow under-turning or over-turning (vectored thrust) produced by the SERN nozzles, whereas the resultant thrust does not. Losses included in both terms are friction drag and pressure drag associated with the nozzle geometry.

The resultant pitch thrust vector angle δ_p is idealistically equal to zero degrees at the design condition for a well designed SERN nozzle. Non-zero values of δ_p are associated with a penalty in axial force because thrust is turned away from the axial centerline. Nonlinear variations in δ_p with

nozzle pressure ratio occur for SERN nozzles because of an unopposed normal force, which varies as the compression-expansion wave patterns change, acting on the large ramp surface. The resulting variations in pitching-moment coefficient must be considered when designing the trim controls of an aircraft with a SERN nozzle.

The nozzle discharge coefficient w_p/w_i is the ratio of measured weight-flow rate determined from upstream venturi measurements, to ideal weight-flow rate, which is calculated from the measured nozzle throat area A_t and, jet total pressure and temperature measurements measured inside the SERN instrumentation section. Discharge coefficient is a measure of the nozzle efficiency in passing weight-flow, and in an actual engine should be held nearly constant to assure efficient engine operation at all flight conditions.

COMPUTATIONAL STUDY

Computational Code

The computational fluid dynamics (CFD) code, PAB3D, solves the three-dimensional, Reynolds-averaged, Navier-Stokes equations (RANS) and implements various turbulence model options (algebraic, two-equation or algebraic Reynolds stress) to close the RANS equations. The flow solver in PAB3D employs three numerical schemes, each constructed with a finite volume approach. The flux-vector splitting scheme of van Leer is used for fast convergence of the implicit terms of the governing and turbulence equations, while the flux-difference splitting scheme of Roe is utilized for solving the explicit terms. A space-marching, modified Roe scheme is implemented for supersonic flows with no imbedded subsonic flow regions or for flows with negligible pressure gradients. A complete description of PAB3D is given in references 11 and 12.

For the present study, two-dimensional (2D) simulations were computed with the Roe and van Leer schemes. A linear, k-ε turbulence model was used with a Jones and Launder damping function (ref. 13) to adjust the turbulent viscosity at the wall. A high Reynolds number form of the k-ε turbulence model was used in the far field.

Performance Calculation

The CFD code contains a performance module (ref. 14) that utilizes the momentum theorem applied to a user-defined control volume to calculate nozzle or aerodynamic performance. Quantities such as lift, drag, thrust, moments, heat transfer and skin friction may be computed for many complex geometric configurations and multi-stream flows. Each quantity is updated throughout the solution development to monitor convergence.

Along flow-through sections of the control volume, mass and momentum fluxes, as well as pressure forces are integrated over each cell with equations 1 and 2.

$$w_p = \Sigma \{\rho U \cdot N\} \Delta A \qquad (1)$$

$$F_{flux} = \Sigma \{\rho U (U \cdot N) + (p - p_\infty) N\} \Delta A \qquad (2)$$

where ΔA is the cell face area and N is the cell face unit vector.

Along solid surfaces of the control volume, skin friction and pressure forces are determined. Surface pressure force $F_{pressure}$ is determined by multiplying cell static pressure by cell face area using equation 3.

$$F_{pressure} = \Sigma [(p - p_\infty) N] \Delta A \qquad (3)$$

The cell surface static pressure is calculated by extrapolating the cell centered static pressure to the surface where the velocity is assumed to be zero.

The skin friction force $F_{friction}$ is calculated with only the velocity gradients normal to the surface contributing to the velocity terms of the viscous stress tensor. A two point difference is used to determine a velocity gradient, one zero-magnitude velocity vector at the surface and a second at the cell center. Sutherland's formula (ref. 15) is used to calculate the dynamic viscosity at the surface by extrapolating the static temperature at a local cell center to the surface and using a reference viscosity and temperature condition. The total body force vector F is defined in equation 4.

$$F = F_{flux} + F_{pressure} + F_{friction} \qquad (4)$$

Computational Domain

The numerical flow field shown in figure 8 for the current model is made up of an internal nozzle duct, an external expansion ramp and a free stream flow field. The internal geometry and expansion ramp were defined with the model design coordinates, but the aerodynamic exterior did not reflect that of the experimental model because the experimental nozzle was tested under static conditions where exterior surfaces are relatively unimportant.

Therefore, it was not desirable to model the actual exterior nozzle hardware.

The computational domain of the concave ramp, low Mach number configuration was defined with 16 blocks. The far field was located 106 throat heights downstream of the nozzle exit, the lower lateral far field was located 88 throat heights below the expansion ramp, and the upper lateral boundary was located 52 throat heights above the expansion ramp. The block defining the throat and expansion ramp had dimensions of 2 x 161 x 85. The boundary layer was defined for a law-of-the-wall coordinate y+ (nondimensional distance of the first grid normal to the surface) of 2 for adequate modeling of the boundary layer flow (ref. 11).

The computational domain of the concave ramp, high Mach number configuration was defined with 20 blocks. The far field was located 206 throat heights downstream of the nozzle exit and the lower and upper lateral boundaries were located 180 throat heights away from the expansion ramp. The block defining the throat and expansion ramp had dimensions of 2 x 181 x 85.

Boundary Conditions

The CFD code has many options for defining the conditions of the inflow, outflow, free stream, wall and centerline boundaries. For this study, Riemann invariants along the characteristics were implemented along the lateral and in-flow free stream boundaries. A constant pressure outflow condition was used at the downstream far field boundary. The nozzle jet conditions were specified with a fixed total temperature and pressure condition. A no-slip adiabatic wall was implemented to obtain a viscous solution.

Grid Study

A grid convergence study was conducted for each predicted solution. Convergence criteria included a decrease of two orders of magnitude in residual and a variance of less than 0.05 percent in discharge coefficient and 0.1 percent in thrust ratio. Additionally, a grid density (mesh) dependence is established through the comparison of converged performance parameters at several grid levels. Initially, the solution was developed on a coarse mesh which contained one sixteenth the total number of base level (fine mesh) grid points. Once the convergence criteria was met, the solution was extrapolated to a medium mesh that included one fourth the total number of base level grid points. Again, the solution was developed until converged, and finally, the solution was extrapolated and converged on the base level grid. Negligible differences between performance parameters obtained from the medium and fine mesh grids are required to ensure a solution independent of mesh density.

PROCESS

The six configurations listed in Table 1 were experimentally tested at static conditions through a NPR range of 2 to 13 in the NASA Langley Jet-Exit Test Facility. Two-dimensional computational solutions were predicted with the Navier-Stokes code, PAB3D, and compared with experimental data for the concave ramp, low Mach number configuration at an overexpanded condition of NPR = 5, at an underexpanded condition of NPR = 13, and at the nominal design point condition, NPR = 9. The CFD code was also used to predict performance at the design condition (NPR_D = 102) of the high Mach number configuration; this condition was unreachable with the experimental model in the test facility. Predicted solutions were computed with near static free-stream conditions.

RESULTS

This study provided an initial assessment of a new SERN nozzle concept through an experimental evaluation at conditions typical of the low Mach number configuration and a computational evaluation at similar test conditions and at conditions unreachable in the static test facility. This allowed for comparison of internal nozzle performance of the intermediate and high Mach number configurations (both of which were highly over-expanded throughout the experimental test range) with the low Mach number configurations whose operating pressure ratio schedule would be typical of the experimental conditions.

Experimental results showing the effect of throat position on axial thrust ratio F_A/F_i is shown in figure 9 for the three nozzle expansion ratios (low, intermediate and high) with concave expansion ramps. As expected, the high Mach number configuration had the lowest thrust ratio over the entire NPR range. The high Mach number configuration was highly overexpanded at all experimental test conditions because of the large expansion ratio (A_e/A_t = 8.25) that had a design point of NPR_D = 102.4. The low Mach number configuration with a smaller expansion ratio (A_e/A_t = 1.83) and a design point of NPR_D = 9, provided an

improvement in axial thrust over the entire range of NPR tested with a 4 percent improvement at very low NPR.

The comparison of predicted axial thrust ratio F_A/F_i with experimental data for the concave ramp, low Mach number configuration is shown in figure 10. The error bars represent an estimate of the experimental uncertainty and the standard deviation of the predicted value over the last 1000 iterations. The magnitude of F_A/F_i was predicted within 1.5 percent of experimental data. Slight over-prediction was expected from the two-dimensional (2D) simulations because they do not model three-dimensional (3D) losses such as separation of the flow from the expansion ramp near the sidewalls, which was evident in the paint-oil flow visualization.

The 3D flow separation mentioned above, occurred along the concave expansion ramp of the low Mach number configuration and was detected in the paint flow patterns at NPR = 13 as shown in figure 11. A vortex pattern was captured downstream of the shock line near the side edges of the expansion ramp where the sidewalls were attached. The 3D effect from the side entrainment of ambient air into the plume is not captured with a 2D computational simulation.

Close similarities exist between the predicted and the experimental flow fields of the concave ramp, low Mach number configuration. The Schlieren photograph in figure 12 shows the experimental density gradients along the centerline of the nozzle, while the CFD predicted Mach contours are presented in figure 13. The model sidewall (see fig. 7) hides the view of the throat region in figure 12 from that shown in figure 13. The thick shear layer, internal oblique shock system, and the separation of the flow from the expansion ramp are apparent in both the experimental data and the computational solution. The predicted shock induced separation shown in the Mach contours near x/L_{ref} = 0.88 is present as a shock line in the paint flow patterns at x/L = 0.87 (fig. 11).

Flow separation observed in the experiment and computations, as well as the variation of compression and expansion waves along the expansion ramp as NPR changes, can result in large moments and resultant pitch thrust vector angles δ_p for SERN nozzles because of the unopposed normal force area of the expansion ramp. Therefore, vehicles employing SERN nozzles would generally have increased trim requirements and trim drag when compared with an equivalent 2DCD nozzle. Experimental results showing the effect of throat location on δ_p are presented in figure 14. Minimal values of δ_p were obtained near the design point (NPR_D = 9) of the concave ramp, low Mach number configuration, while the high Mach number configuration had a resultant pitch thrust vector angle of δ_p = - 6.5 degrees at this condition. Figure 15 shows the comparison of predicted δ_p at nozzle pressure ratios of 5, 9, and 13 with experimental data for the concave ramp, low Mach number configuration (uncertainty included with error bars). The trend and magnitude of δ_p were predicted within 3 degrees. Both the experiment and the computation favorably produced $\delta_p \approx 0$ degrees at the design condition, NPR_D = 9.

The low Mach number configuration is used to demonstrate the effect of expansion ramp design (concave vs. convex) on internal nozzle performance because the test range of NPR was typical of the operating range for this configuration. Figure 16 shows a comparison of F_A/F_i and δ_p for the concave and convex expansion ramp designs. The concave ramp geometry provided higher axial thrust ratios over most of the NPR test range. The axial thrust ratio increase was about 6.5 percent at the design NPR of 9. Additionally, the convex design produced a resultant pitch thrust vector angle of δ_p = 17.5 degrees, while the concave design had $\delta_p \approx 0$ degrees the design NPR. The convex design had a positive initial expansion angle that vectored the flow downward from the axial centerline while the concave design had a negative initial expansion angle that encouraged the expansion along the ramp (see fig. 4). The convex design provided a primarily normal projected area within one inch of the throat, such that an increase in pressure ratio resulted primarily in an increase in normal force and correspondingly, resulted in large δ_p increments. The concave design had a projected area in the normal and the axial directions, such that an increase in pressure resulted in an increase in both normal and axial force components and therefore, the variations in δ_p were smaller.

Experimental data for the concave ramp, low Mach number configuration was used to validate the code at NPRs of 5, 9, and 13. The code was then utilized to predict the internal nozzle performance of the concave ramp, high Mach number nozzle at the design condition, NPR_D = 102. The predicted axial thrust ratio was $F_A/F_i = 0.886 \pm 0.001$, the resultant thrust ratio was $F_r/F_i = 0.906 \pm 0.001$, the discharge coefficient was $w_p/w_i = 0.939 \pm 0.001$, and the resultant pitch thrust vector angle was $\delta_p = 12.08 \pm 0.12$ degrees. The solution performance convergence history for this condition is shown in figure 17. Performance parameters are plotted versus iteration to

monitor convergence throughout the solution development.

The predicted Mach contours for the concave ramp, high Mach number configuration at NPR_D = 102 are shown in figure 18. Underexpanded flow at the trailing edge of the lower flap continues to expand to ambient pressure through an expansion fan of approximately 60 degrees. The thick shear layer and the expansion waves from flow expanding around the geometric discontinuities on the expansion ramp are evident. The internal oblique shock near the trailing edge of the ramp may have resulted from overexpanded nozzle conditions or from the reflex in ramp geometry (near x/L_{ref} = 0.91) compressing supersonic flow. The predicted pressure ratios upstream and downstream of the shock correspond to local Mach numbers of M = 4.4 and M = 3.8, respectively. The estimated downstream Mach number for a local deflection angle of 3.4 degrees at M = 4.4 is M ≈ 4. A computational sweep in Mach number would clarify if the internal oblique shock resulted from the expansion ramp geometry or from overexpanded conditions.

The grid density study for the high Mach number nozzle at the design condition is shown in figure 19. Although axial thrust ratio changed 0.3 percent from the coarse to the medium mesh refinement, the difference from the medium to fine mesh refinement was only 0.04 percent. The resultant pitch thrust vector angle changed 3.8 percent at the medium mesh refinement, but only 0.77 percent at the fine mesh refinement. Finally, the discharge coefficient changed 0.2 percent and 0.01 percent at the medium and fine mesh refinements, respectively. The negligible changes at the fine mesh refinement are important because this indicates a solution independent of mesh density.

CONCLUSIONS

A static investigation was conducted in the NASA Langley Jet-Exit Test Facility. Experimental results were verified with the computational fluid dynamics code, PAB3D. The results from the computational investigation supported both the performance data from the experiment and the flow characteristics observed with paint flow and focusing Schlieren flow visualization techniques. The results from this investigation indicate the following.

1. An improvement in axial thrust ratio occurred when the nozzle throat was translated to provide a more ideal expansion ratio for a given set of operating conditions. At low nozzle pressure ratios, the concave ramp, low Mach number configuration provided a 4 percent improvement in axial thrust ratio compared to the concave ramp, high Mach number configuration.

2. Experimental values of axial thrust ratio were predicted within 1.5 percent at nozzle pressure ratios of 5, 9 and 13 using a two-dimensional computational domain to model the concave ramp, low Mach number nozzle.

3. Remarkable similarities between computational and experimental flow characteristics were obtained in this study, including the plume shear layers, internal oblique shock system, and separation of the flow from the expansion ramp.

4. Improvement in resultant pitch thrust vector angle resulted from translating the nozzle throat to a more appropriate expansion ratio (closer to design). The concave ramp, low Mach number configuration provided minimal values of resultant pitch thrust vector angle, $\delta_p \approx 0$, at the design nozzle pressure ratio, $NPR_D = 9$.

5. The concave expansion ramp design provided a more ideal expansion surface than the convex expansion ramp design for the low Mach number configuration. Axial thrust ratio was 6.5 percent higher and resultant pitch thrust vector angle was approximately zero for the concave design at the design nozzle pressure ratio.

REFERENCES

1. Kuchar, A. P.; and Wolf, J. P.: Preliminary Assessment of Exhaust Systems For High Mach (4 to 6) Fighter Aircraft. AIAA 89-2356, July 1989.

2. Dusa, D. J.: Turboramjet Exhaust Nozzle Systems. X ISABE, September 1-6, 1991.

3. Carboni, Jeanne D.; Shyne, Rickey J.; Leavitt, Laurence D.; Taylor, John G.; and Lamb, Milton: *Supersonic Investigation of Two-Dimensional Hypersonic Exhaust Nozzles*. NASA TM-105687, October 1992.

4. Capone, Francis J.; Re, Richard J.; and Leavitt, Laurence D.: *Parametric Investigation of Single-Expansion-Ramp Nozzles at Mach Numbers From 0.6 to 1.2.* NASA TP-3240, October 1992.

5. Bare, E. Ann; and Capone, Francis J.: *Static Internal Performance of Convergent Single-Expansion-Ramp Nozzles With Various Combinations of Internal Geometric Parameters.* NASA TM-4112, May 1989.

6. Re, Richard J.; and Leavitt, Laurence D.: *Static Internal Performance of Single-Expansion-Ramp Nozzles With Various Combinations of Internal Geometric Parameters.* NASA TM-86270, December 1984.

7. A User's Guide to the Langley 16-Foot Transonic Tunnel Complex, Revision 1. NASA TM-102750, September 1990. (Supersedes NASA TM-83186.)

8. Maltby, R. L.: and Keating, R. F. A., compilers: The Surface Oil Flow Technique for Use in Low Speed Wind Tunnels. *Flow Visualization in Wind Tunnels Using Indicators.* AGARDograph 70, April 1962, pp. 29-38.

9. Weinstein, Leonard M.: An Improved Large-Field Focusing Schlieren System. AIAA 91-0567, January 1991.

10. Mercer, Charles E.; Berrier, Bobby L.; Capone, Francis J.; and Grayston, Alan M.: *Data Reduction Formulas for the 16-Foot Transonic Tunnel NASA Langley Research Center, Revision 2.* NASA TM 107646, 1992.

11. Abdol-Hamid, Khaled S.; Lakshmanan, B.; and Carlson, John R.: *Application of Navier-Stokes Code PAB3D With k-ε Turbulence Model to Attached and Separated Flows.* NASA TP-3480, January 1995.

12. Abdol-Hamid, Khaled S.: *Implementation of Algebraic Stress Models in a General 3-D Navier-Stokes Code Method (PAB3D).* NASA CR-4702, December 1995.

13. Jones, W. P.; and Launder, B. E.: The Prediction of Laminarization With a Two-Equation Model of Turbulence. *Int. Journal of Heat & Mass Transfer*, vol. 15, no. 2, February 1972, pp. 301-314.

14. Carlson, John R.: *A Nozzle Internal Performance Prediction Method.* NASA TP-3221, October 1992.

15. Ames Res. Staff: *Equations, Tables, and Charts for Compressible Flow.* NACA Rep. 1135, 1953.

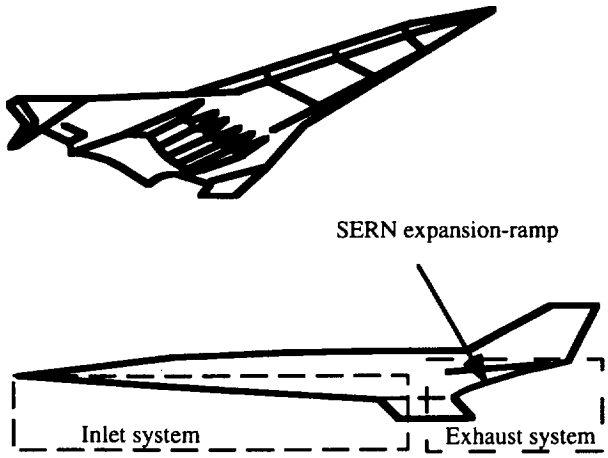

Figure 1. Sketch of a highly integrated high speed vehicle.

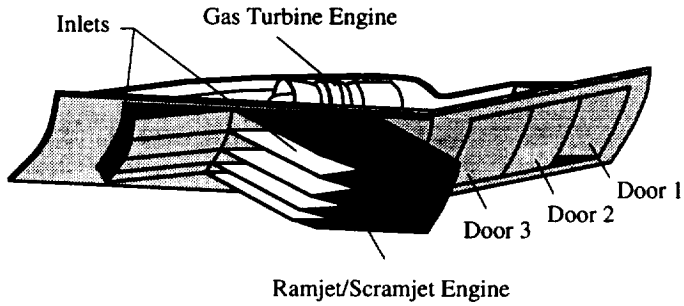

Figure 2. Translating throat single expansion-ramp nozzle integrated into the afterbody of a high-speed vehicle.

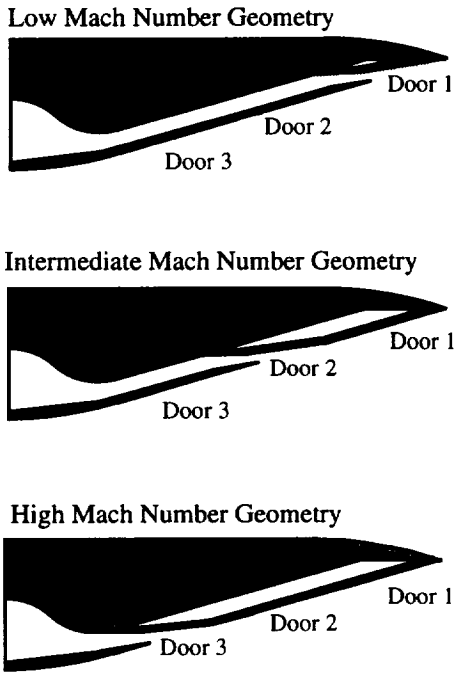

Figure 3. Sketch of the translating throat single expansion-ramp nozzle model.

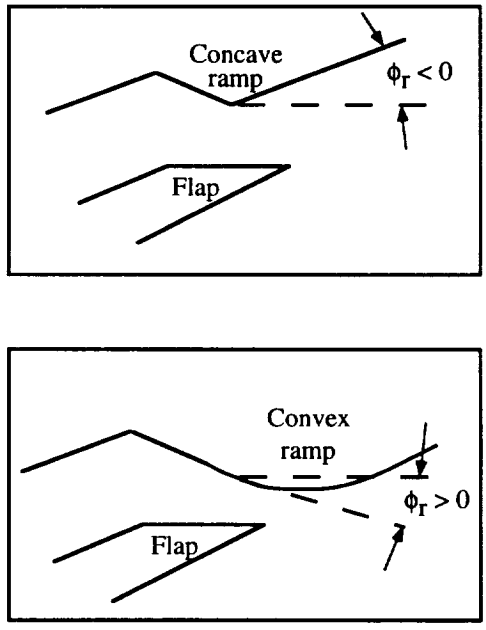

Figure 4. Comparison of the concave and convex expansion-ramp design near the throat. Sign convention for the initial expansion angle ϕ_r.

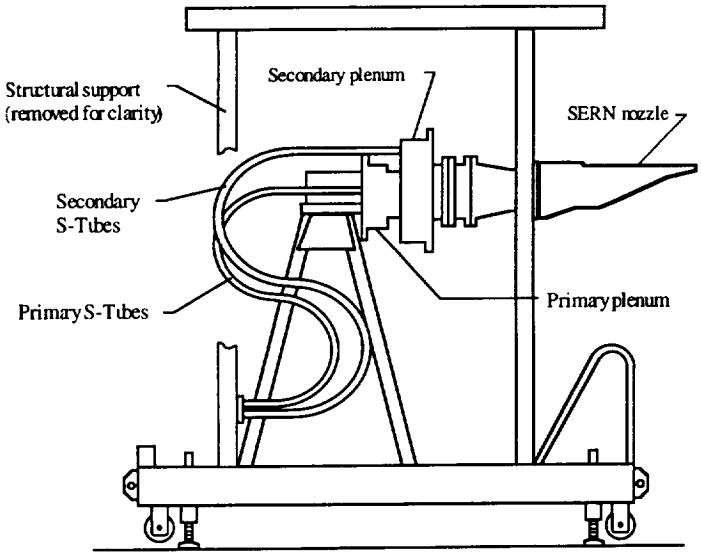

Figure 5. Sketch of the dual-flow, single engine, propulsion simulation system attached to the A-frame structural support cart.

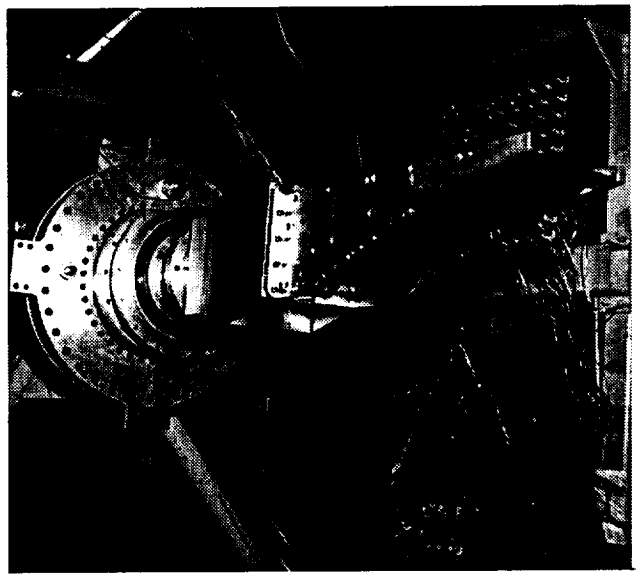

Figure 6. Photograph of the concave ramp high Mach number configuration installed on the dual-flow propulsion simulation system.

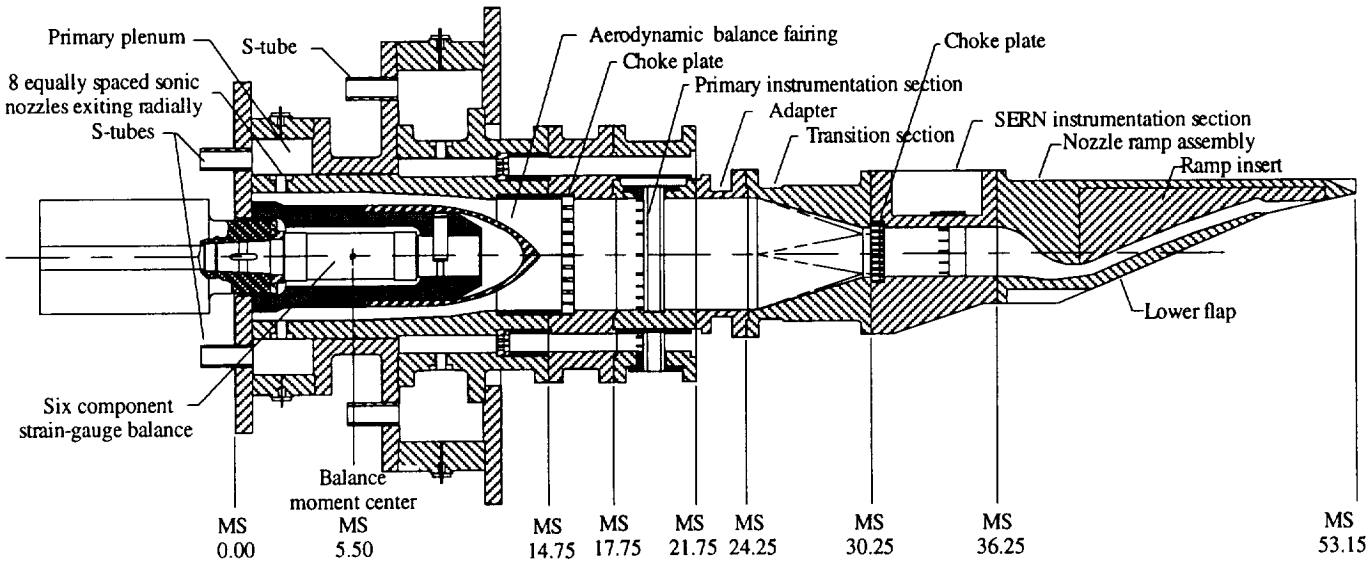

Figure 7. Sketch of a typical translating throat SERN configuration installed on the dual-flow propulsion simulation system.

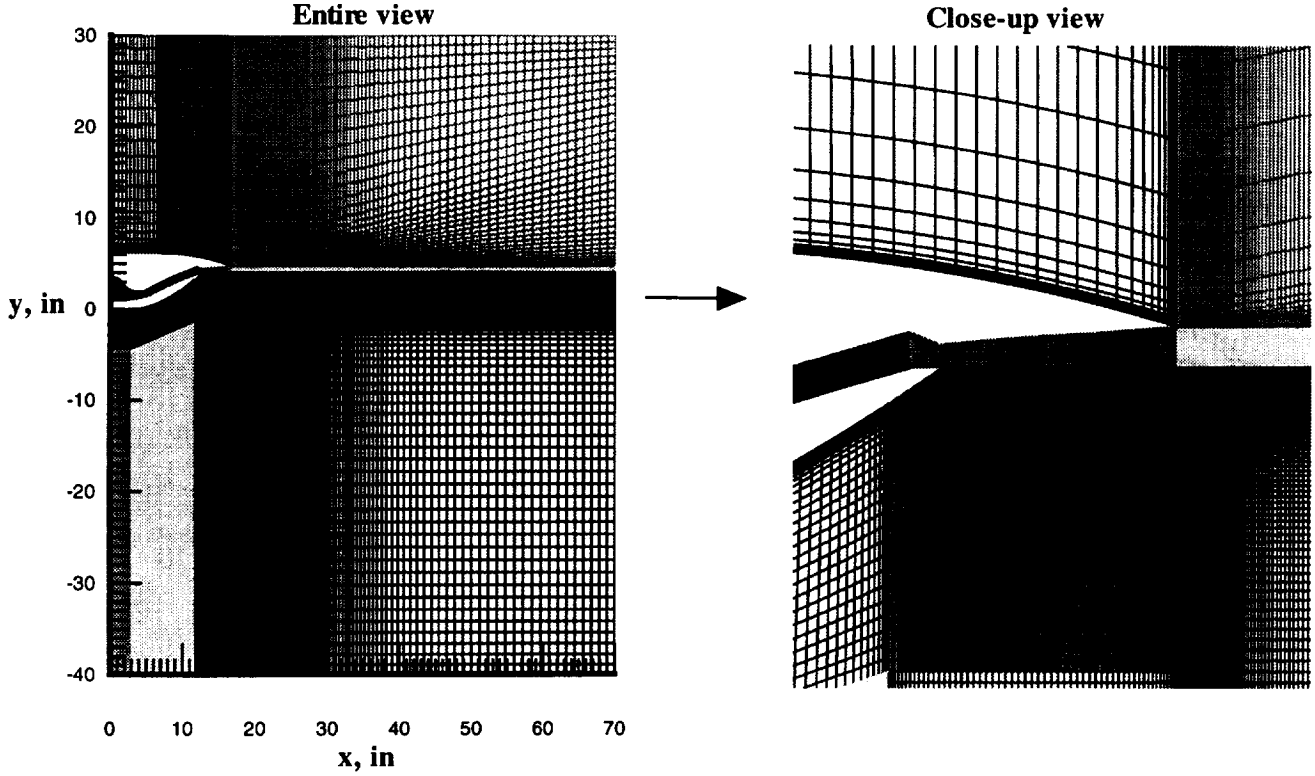

Figure 8. Computational domain for the concave ramp, low Mach number configuration.

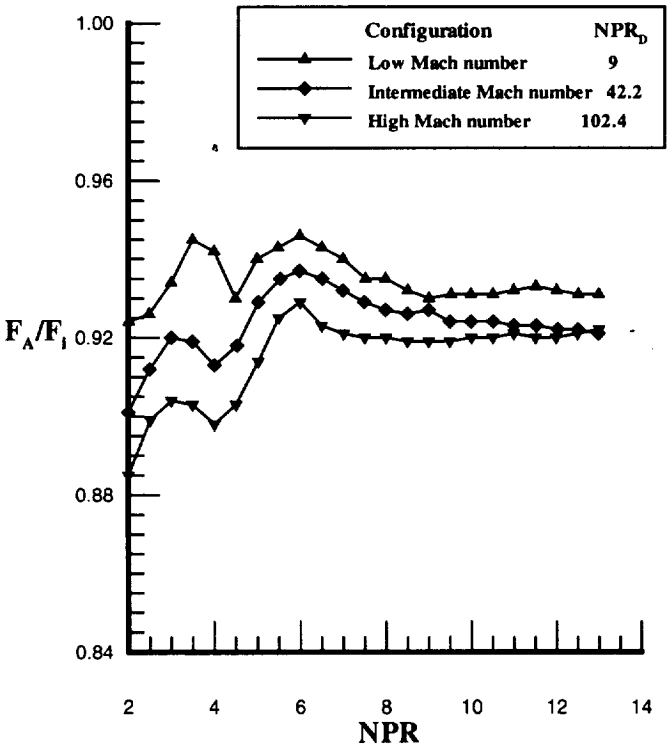

Figure 9. Experimental results showing the effect of throat position on axial thrust ratio for the configurations with the concave ramp design.

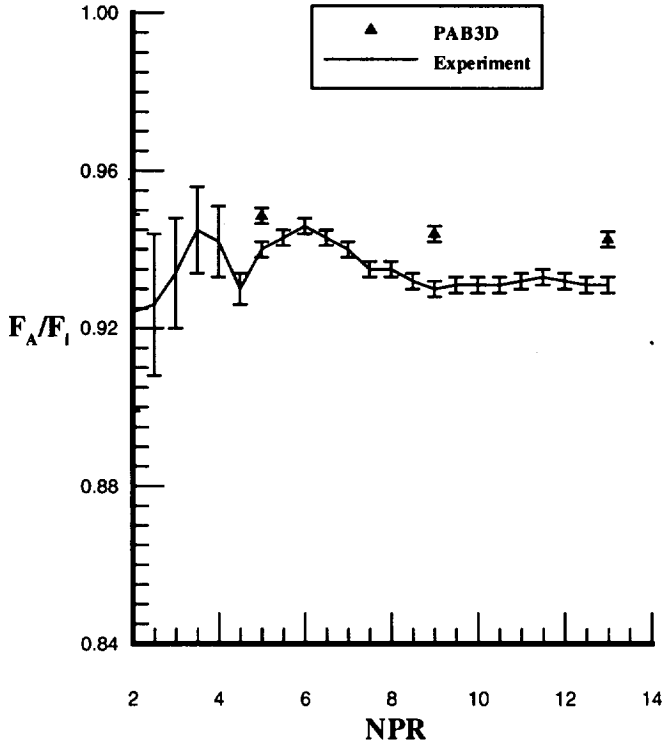

Figure 10. Comparison of predicted axial thrust ratio with experimental data for the concave ramp, low Mach number configuration. Uncertainty represented with error bars.

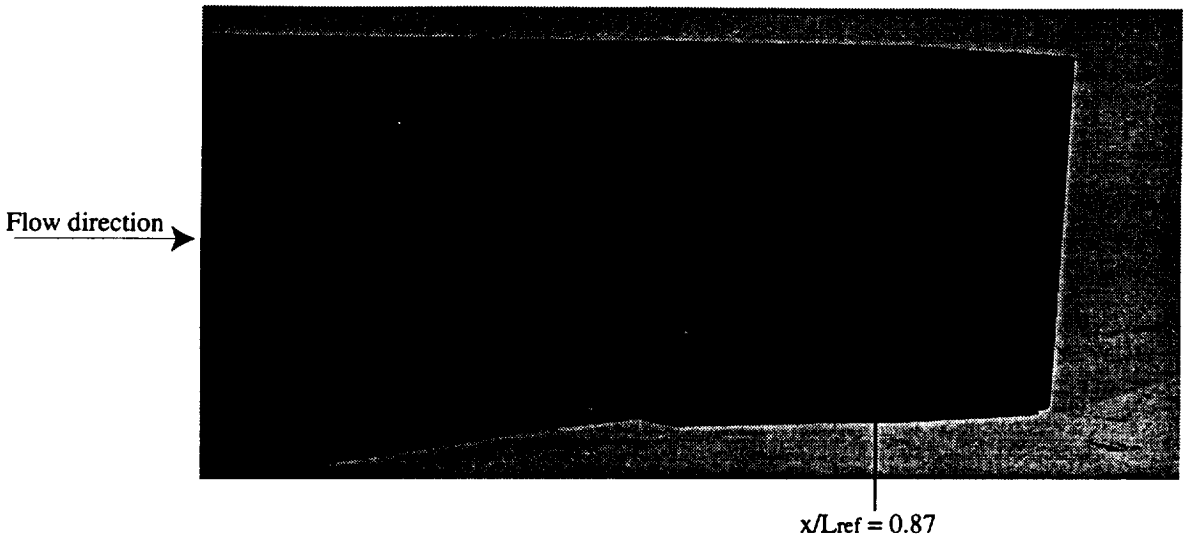

Figure 11. Paint-oil flow pattern along the concave ramp of the low Mach number configuration at NPR = 13.

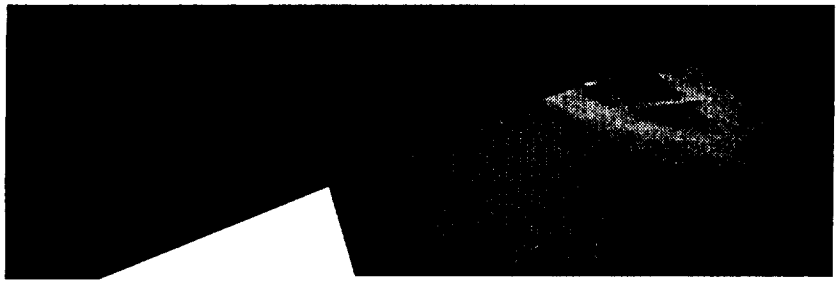

Figure 12. Schlieren photograph of the density gradients along the concave ramp of the low Mach number configuration at NPR = 13.

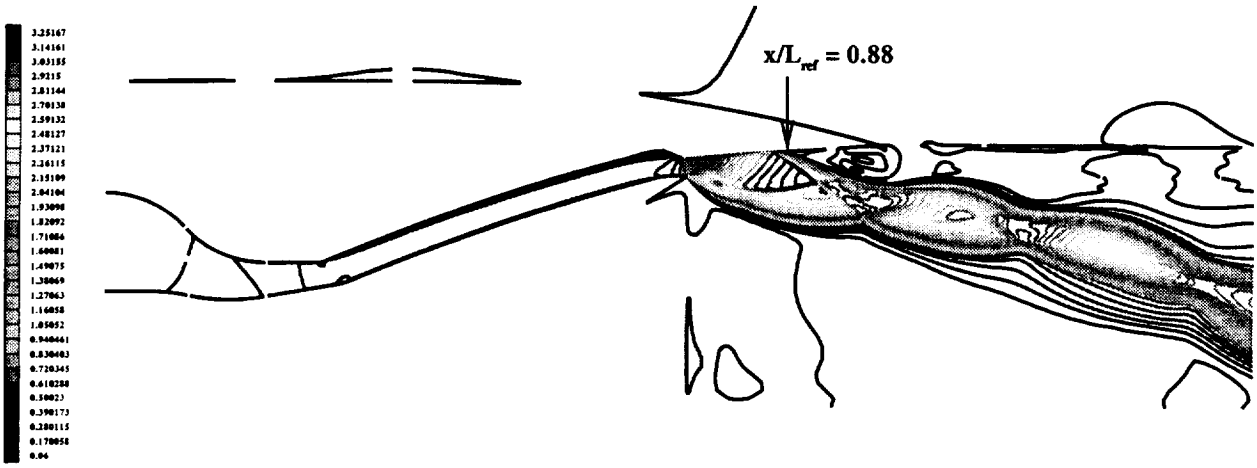

Figure 13. Predicted Mach contours for the concave ramp, low Mach number configuration at NPR = 13.

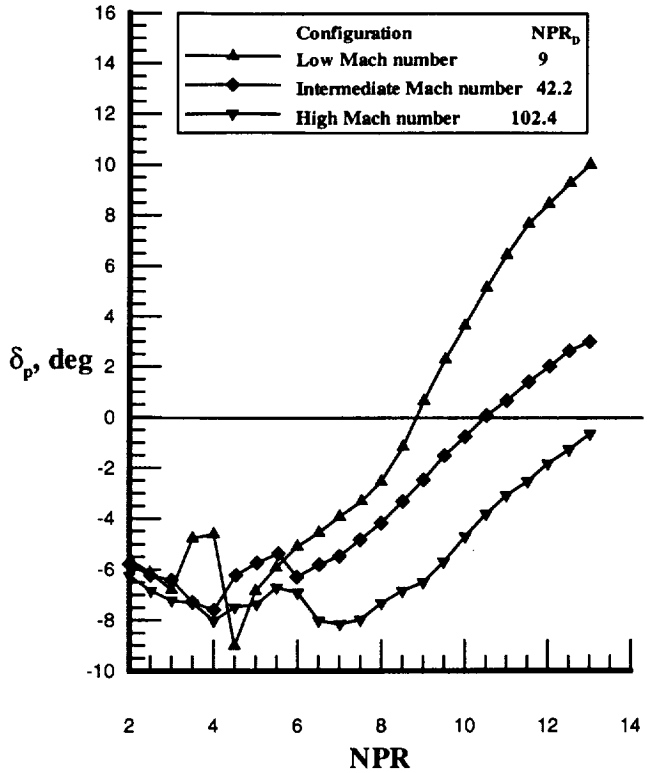

Figure 14. Experimental results showing the effect of axial throat location on resultant pitch thrust vector angle.

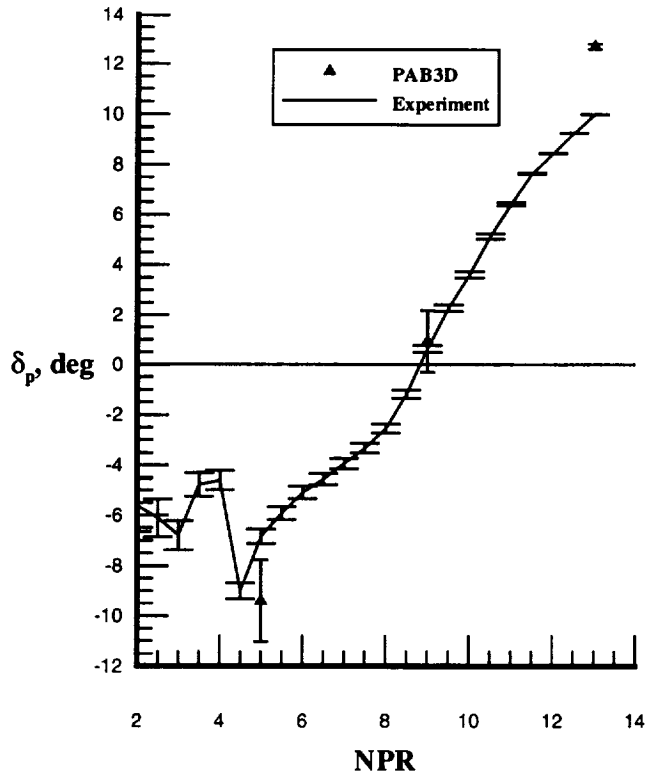

Figure 15. Comparison of predicted resultant pitch thrust vector angle with experimental data for the concave ramp, low Mach number configuration. Uncertainty represented with error bars.

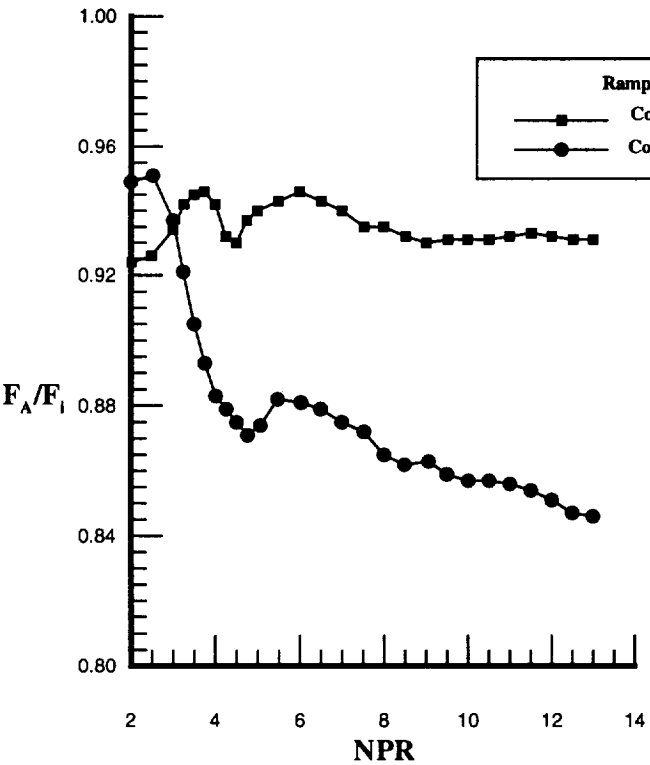

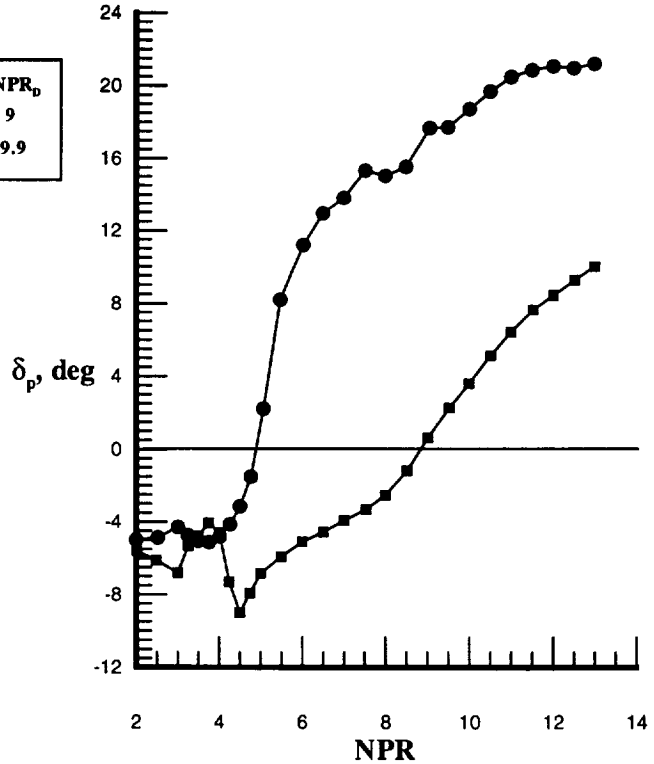

Figure 16. Effect of expansion-ramp design (concave vs. convex) on internal performance of the low Mach number configurations.

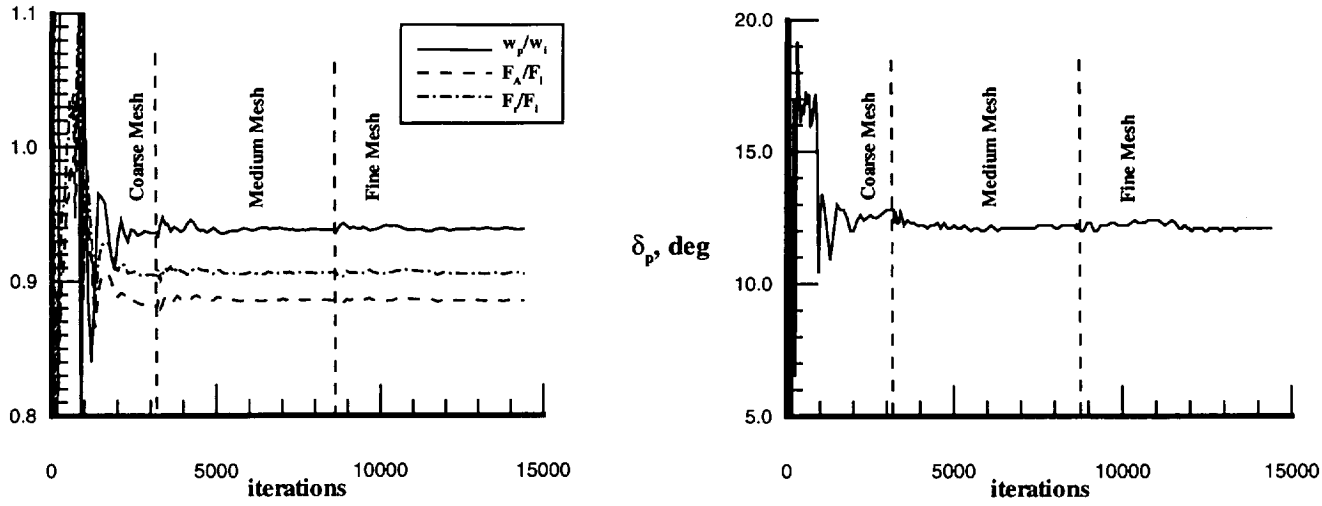

Figure 17. Solution performance convergence history for the concave ramp, high Mach number configuration at M = 0.1 and NPR = 102.

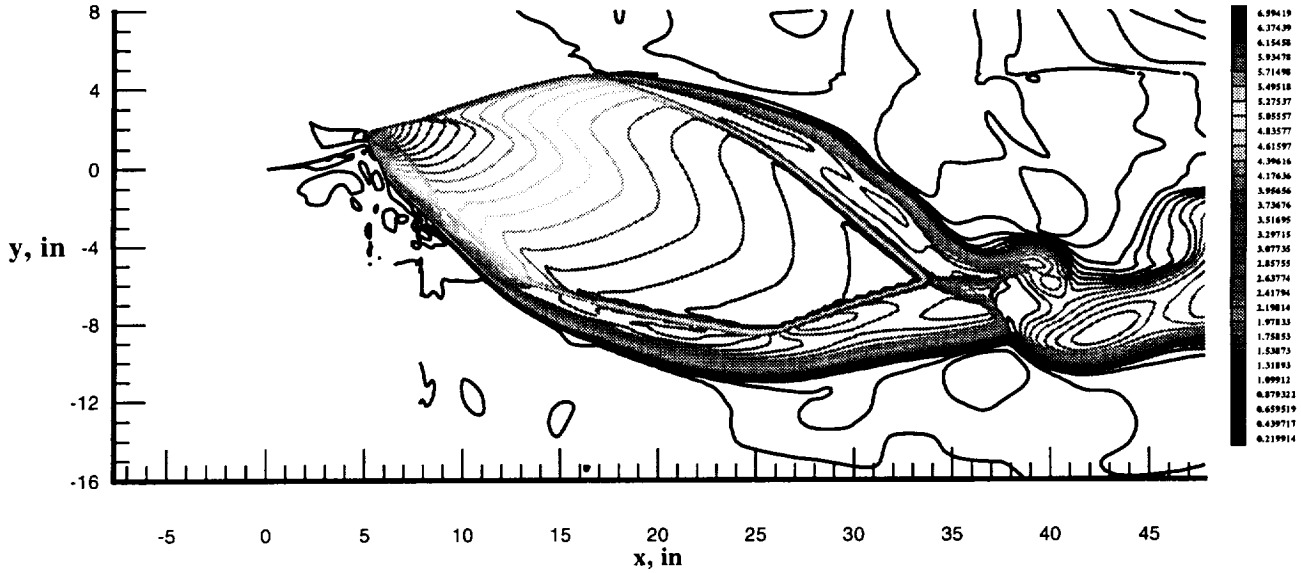

Figure 18. Predicted Mach contours along the centerline of the concave ramp, high Mach number configuration at M = 0.1 and NPR = 102.

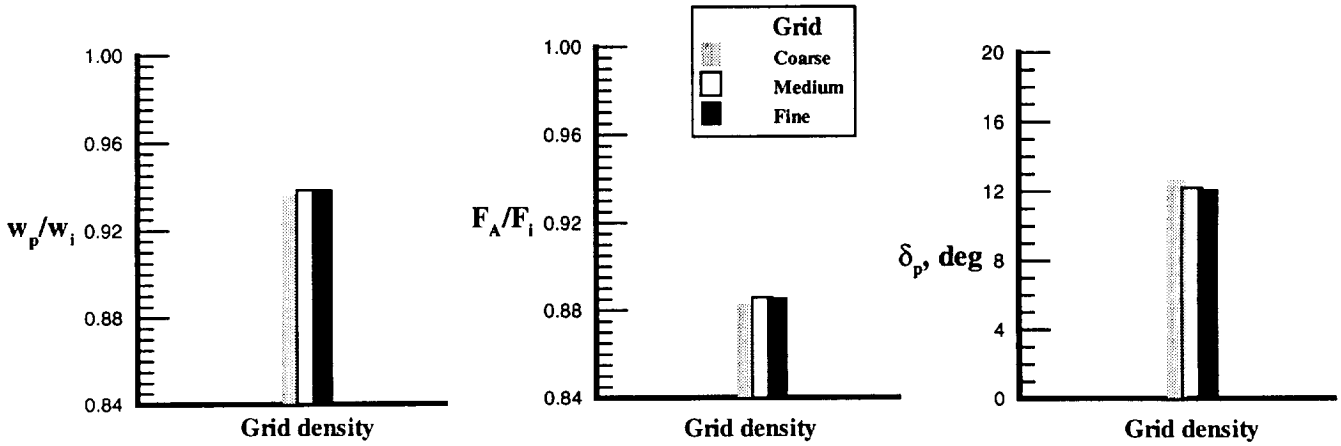

Figure 19. Effect of grid density on performance quantities for the concave ramp, high Mach number configuration at M = 0.1 and NPR = 102.